

1 **A measurement and model study on ozone characteristics in marine air at a remote**

2 **island station and its interaction with urban ozone air quality in Shanghai, China**

3 Yixuan Gu^{a,b}, Fengxia Yan^c, Jianming Xu^{a,b,*}, Yuanhao Qu^{a,b}, Wei Gao^{a,b}

4 ^aShanghai Typhoon Institute, Shanghai Meteorological Service, Shanghai 200030, China

5 ^bShanghai Key Laboratory of Meteorology and Health, Shanghai Meteorological Service,

6 Shanghai 200030, China

7 ^cMeteorological Center of Traffic Management of East China, Shanghai 2000135, China

8 Corresponding to: Dr. Jianming Xu (metxujm@163.com)

9

10 Keywords: Ozone in oceanic air, Urban Plume, Coastal city air pollution, Shanghai

11 **Abstract**

12 To understand the characteristics and changes of baseline ozone (O_3) in oceanic air in
13 East China, a six-year measurement of O_3 concentration was conducted from January 1
14 2012 to September 15 2017 at a remote offshore station located on the Sheshan Island
15 (SSI) near the megacity of Shanghai. The observed monthly mean O_3 concentrations at
16 SSI ranged from 33.4 to 61.4 ppbv during the study period, which were about 80% and 12%
17 higher, respectively than those measured at downtown and rural sites in Shanghai.
18 Compared to the remarkable O_3 increases observed at urban and rural sites in Shanghai,
19 observed O_3 concentrations at SSI exhibited statistically insignificant increasing changes
20 ($1.12 \text{ ppbv yr}^{-1}$, $\alpha > 0.10$) during the observation period, suggesting less impacts of
21 anthropogenic emissions on O_3 levels in oceanic air. In addition, an insignificant
22 decreasing change ($-0.72 \text{ ppbv yr}^{-1}$, $\alpha > 0.10$) was detected in O_3 concentrations at SSI in
23 September and October when the influence of regional transport was minimum
24 throughout the year, providing a good proxy to study the baseline oxidation capacity of the
25 oceanic atmosphere. City plumes from Shanghai usually carried higher levels of NO_x ,
26 resulting in decreased O_3 concentrations at SSI during southwesterly and westerly winds.
27 However, In MAM (March–May) and JJA (June–August), due to the enhanced production
28 of oxygenated volatile organic compounds, O_3 could be continuously produced during
29 daytime in aged city plumes, resulting in elevated O_3 concentrations transported to SSI.
30 The impacts of the offshore O_3 on O_3 levels in Shanghai are quantified during an easterly
31 wind dominant episode (September 1–30, 2014) using the WRF-Chem model. Sensitivity
32 results suggest that O_3 in the oceanic air inflows can lead to 20–30% increases in urban

33 O₃ concentrations, which should be crucially considered in dealing with urban O₃ pollution
34 in large coastal cities like Shanghai.

35 1 Introduction

36 Ground-level ozone (O_3) is a harmful photochemical oxidant detrimental to air quality,
37 human health and land ecosystems (Yue and Unger 2014; Monks et al., 2015; Li et al.,
38 2019a). High ambient O_3 has been proved to increase the risks of respiratory and
39 cardiovascular mortality (Goodman et al., 2015) and enhance the greenhouse effect
40 (IPCC, 2013). In recent years, O_3 pollution has drawn increasing attention in China, since
41 O_3 pollution is getting worse in spite of the implementation of Chinese Clean Air Action
42 Plan. In contrast to the 28-40% decreases in $PM_{2.5}$ (fine particulate matter; diameter ≤ 2.5
43 μm) levels, the observed daily maximum 8-h average (MDA8) O_3 concentrations show
44 increasing rates of 1–3 ppb yr^{-1} in summer in megacities over eastern China during 2013–
45 2017 (Li et al., 2019b). To address the underlying causes of the increasing O_3 pollution
46 has become an urgent issue that triggers lots of discussions based on observational and
47 model studies worldwide (Yang et al., 2014; Lou et al., 2015; Fu et al., 2019).

48 Observational and model studies indicated that the elevated O_3 levels in urban and
49 rural areas in eastern China were strongly related to the changes in anthropogenic
50 emissions of O_3 precursors (Ma et al., 2016; Lu et al., 2018; Li et al., 2019b; Gu et al.,
51 2020). Since the O_3 formation was reported to be under volatile organic compound (VOC)
52 limited regime in most Chinese megacities (e.g. Beijing, Shanghai, and Guangzhou), the
53 sharp decreases in nitrogen oxides ($NO_x=NO+NO_2$) emissions combined with slight
54 increases in VOC levels were suggested to be main causes of the observed enhancement
55 of O_3 concentrations in East China (Gao et al., 2017; Xu et al., 2019). In remote areas,
56 changes of baseline O_3 also exhibit sensitive responses to human activities (Vingarzan,

57 2004; Meng et al., 2009; Wang et al., 2009; Lin et al., 2015). Based on 14-year
58 observations at a coastal site in Hong Kong, Wang et al. (2009) pointed out that enhanced
59 pollution flow from the upwind coastal regions contributed to most of the observed O₃
60 increases in the background atmosphere of South China during 1994–2007. And the
61 increase in background O₃, in turn, made a strong contribution of 81% to the increasing
62 rate of O₃ in urban Hong Kong. It is thus necessary to understand the background O₃
63 changes and their responses to different sources when developing long-term strategies to
64 mitigate local O₃ pollution. However, compared to the intensive field studies in polluted
65 cities and surrounding rural regions, continuous observations of O₃ at representative
66 background sites in China are relatively limited (Wang et al., 2017).

67 To better understand the characteristics of the background O₃ changes in mainland
68 China, the China Meteorological Administration (CMA) started to conduct continuous
69 measurements of surface O₃ at several regional background stations (e.g. Shangdianzi,
70 Linan, and Longfengshan) since 2005. Over 10-year records from those sites and
71 Waliguan, a baseline Global Atmospheric Watch (GAW) station in Tibetan Plateau region,
72 exhibited different increases in background continental O₃ concentrations especially
73 during daytime in China (Lin et al., 2008; Xu et al., 2008; Meng et al., 2009; Ma et al.,
74 2016; Xu et al., 2016). The detected positive trends of O₃ were in a range of 0.24–1.13
75 ppbv yr⁻¹, suggesting enhanced atmospheric oxidation capacity of continental air
76 responding to the rapid development of urbanization and industrialization in the past
77 decades. In addition to the changes at background O₃ in terrestrial stations mentioned
78 above, the characteristics of baseline O₃ at remote marine sites are also important. It is

79 because that large amounts of O_3 pollution events occurred in coastal urban
80 agglomerations in East China (Lu et al., 2018; Li et al., 2019a, b), affected by both city
81 plumes and oceanic air inflows (Tie et al., 2009; Shan et al., 2016). For example, model
82 work of Tie et al. (2009) suggested that sea air masses carried by oceanic inshore air
83 flows aggravated urban O_3 pollution in Shanghai under convergence conditions.
84 Understanding the O_3 characteristics in offshore oceanic regions is therefore an important
85 prerequisite for understanding the land-sea O_3 interactions and its impacts on O_3 pollution
86 in coastal cities. However, to our knowledge, studies on the characteristics and changes
87 of O_3 in marine air are quite limited in mainland China since it is very difficult to conduct
88 systematic and continuous observations under remote oceanic air conditions.

89 In this report, we present the first relatively long and continuous measurements of O_3
90 conducted on a remote offshore island (Sheshan Island, SSI) from January 2012 to
91 September 2017 in eastern China. The SSI is located at the confluence of the Yellow Sea
92 and the East China Sea, covering an area of about 0.4 km^2 . Since there are no inhabitants
93 in the island, the observed O_3 is seldom affected by local anthropogenic emissions. The
94 collected O_3 data are used to understand the levels and variabilities of O_3 in the offshore
95 regions and their impacts on the O_3 concentrations in coastal city areas. First shown are
96 the general impacts of regional transport on the remote atmosphere over the SSI region.
97 Then the diurnal patterns of O_3 at SSI are investigated by comparing them with those
98 observed at a downtown site (XJH) in Shanghai. Multi-year changes of O_3 concentrations
99 at SSI are analyzed to examine the overall changes of baseline O_3 in marine air and
100 possible causes. Also analyzed are the impacts of urban plumes on O_3 levels in oceanic

101 air in offshore regions. At last, the influence of O₃ carried by oceanic air inflows on urban
102 O₃ air quality in Shanghai is assessed using the Weather Research and Forecasting
103 model coupled with Chemistry (WRF-Chem).

104 2 Material and methods

105 2.1 The SSI site and ozone observations

106 To investigate the characteristics and variabilities of O₃ in marine air and their interactions
107 with urban air quality in coastal areas, ground O₃ concentrations were continuously
108 measured at SSI site (31.4°N, 122.3°E, 73.5 m a.s.l.), which is approximately 75
109 kilometers away from the east edge of Shanghai city. Figure 1 shows the location of SSI
110 and the surrounding environment. As mentioned in Sect. 1, there is no resident and tourist
111 on the island. The observed O₃ at SSI site can represent the background O₃ conditions in
112 oceanic air which are seldom contaminated by anthropogenic emissions. Hourly O₃ data
113 was collected during January 1 2012 to September 15 2017, with a capture rate of 89.7%.
114 O₃ was measured using an analyzer from Ecotech, Australia (Model EC9810), which
115 combined microprocessor control with ultraviolet photometry. The instrument met the
116 technical specifications for United States Environmental Protection Agency, with a quality
117 control check every 3 days, filter replaced every 2 weeks and calibration every month.

118 2.2 Observational data at urban and rural sites in Shanghai

119 To better understand the characteristics of the offshore O₃ in oceanic air at SSI, O₃
120 observations obtained from a downtown site, Xujiahui (XJH) are used for comparisons.
121 The XJH site is located at downtown Shanghai, approximately 80 km west from the SSI.
122 Since measurements of NO_x, carbon monoxide (CO) and meteorological parameters (e.g.

123 wind direction and wind speed) were unavailable at SSI, observations obtained at an
124 adjacent site, Dongtan (DT), are substituted for the investigation. The DT site was set up
125 in a national nature reserve near the coast of Shanghai, where the observed pollutant
126 levels have been reported to well reflect the impacts of megacities in the Yangtze River
127 Delta (YRD) region on the remote atmosphere during the MIRAGE-Shanghai (Megacities
128 Impact on Regional and Global Environment at Shanghai) field campaign (Tie et al., 2013).
129 Similar to SSI, the DT site is also little affected by human activities. The obtained
130 observations of meteorology and pollutants are therefore applied for analyzing the
131 impacts of regional transport on observed O₃ concentrations at SSI. NO_x concentrations
132 were measured with a chemiluminescent trace level analyzer (TEI; Model 42iTL), with
133 detection limit of 0.025 ppb. CO concentrations were measured by the Model 48iTL
134 Enhanced CO analyzer, based on gas filter correlation technology. The wind speed and
135 wind direction were measured by using a DZZ4 Automatic Weather Station certificated by
136 the China Meteorological Administration. The geographical locations and surrounding
137 environment of XJH, DT, and SSI are displayed in Fig. 1.

138 2.3 The WRF-Chem model

139 We simulate O₃ using the regional chemical transport model WRF-Chem (version 3.8,
140 <https://www2.acom.ucar.edu/wrf-chem>), collaboratively developed through efforts of
141 several institutes, such as the National Center for Atmospheric Research (NCAR) and the
142 National Oceanic and Atmospheric Administration (the National Centers for Environmental
143 Prediction (NCEP). The model includes on-line calculation of meteorological parameters,
144 transport, mixing, emission, and chemical transformation of trace gases and aerosols

145 (Grell et al., 2005). The Regional Acid Deposition Model version 2 (RADM2, Stockwell et
146 al., 1990) gas-phase chemical mechanism is used for the O_3 formation chemistry.
147 Photolysis rates are calculated by using the fast radiation transfer module (FTUV)
148 followed those in Madronich and Flocke (1999) and Tie et al. (2003). ISORROPIA II
149 secondary inorganic (Fountoukis and Nenes, 2007) and the Secondary ORGanic Aerosol
150 Model (SORGAM) (Schell et al., 2001) schemes are used for aerosol chemistry. Dry
151 deposition follows the standard resistance-in-series model of Wesely (1989). The major
152 physical processes employed in the model follow the Lin microphysics scheme (Lin et al.,
153 1983), the Yonsei University (YSU) planetary boundary layer (PBL) scheme (Hong and
154 Lim, 2006), the Noah Land surface model (Chen and Dudhia, 2001), and the long-wave
155 radiation parameterization (Dudhia, 1989).

156 The model used in this study has a horizontal resolution of 6km \times 6km, including 150
157 un-staggered grids in west-east, 150 un-staggered grids in south-north, and 35 vertical
158 layers extending from the surface to 50 hPa. The domain encompasses Shanghai and its
159 surrounding region, centered at 31.3°N, 121.4°E. The NCEP FNL (Final) Operational
160 Global Analysis data are used for meteorological initial and boundary conditions, with
161 lateral meteorological boundary updated every 6 h. Basic chemical lateral boundary
162 conditions are constrained by a global chemical transport model (MOZART-4, Model for
163 OZone And Related chemical Tracers, version 4) (Tie et al., 2001; Emmons et al., 2010).
164 Anthropogenic emissions are derived from the Multi-resolution Emission Inventory for
165 China (MEIC inventory, <http://www.meicmodel.org/>; Li et al., 2014) for year 2010. Biogenic
166 emissions are calculated online using model of emissions of gases and aerosols from

167 nature (MEGAN2, Guenther et al., 2006).

168 2.4 Methods for assessing the trend of ozone

169 The daily mean O₃ concentrations are used to examine the overall changes in O₃

170 concentrations during the period 2012–2017, including all time of day with qualified

171 measurements. The trends are assessed using two nonparametric methods, which are

172 commonly used to detect trends of non-normally distributed data with seasonality (Xu et

173 al., 2016).The Mann-Kendall (MK) trend test (Mann, 1945; Kendall, 1975; Gilbert, 1987) is

174 used to examine the trend significance, and the Theil-Sen trend estimate method (Sen,

175 1968) is used to estimate the slope of trend, which could also be considered as the rate of

176 change, during the six-year period. Compared to the linear fitting analysis which requires

177 data to be independent and follow a Gaussian distribution, the non-parametric trend test

178 methods only need the data to be independent (Gocic and Trajkovic, 2013). To determine

179 if the calculated rate of change is statistically significant, the confidence level of at least 95%

180 is adopted in the MK trend test, with α value less than 0.05 being considered a statistically

181 significant trend. The trend significance is examined by comparing the value of a

182 standardized test statistic Z to that of a standard normal variate at a given significance

183 level (Z_α , $\alpha=0.05$). If $|Z| > Z_{1-\alpha/2}$, then the dataset is non-stationary, exhibiting either an

184 increasing or a declining trend; If $|Z| \leq Z_{1-\alpha/2}$, then the dataset is stationary with no

185 significant trend. Detailed calculation of Z can be referred to Xu et al. (2016).

186 3 Results and discussion

187 3.1 Regional transport characteristics at SSI

188 The observed O₃ concentrations at SSI were inevitably influenced by regional transport

189 depending on the prevailing winds in various seasons. Figure 2 displays the monthly wind
190 rose diagrams averaged over the period of 2012 to 2017 at DT. As mentioned in Sect. 2.2,
191 the DT site is a rural site located quite close to SSI. The observed wind speeds and wind
192 directions could then be applied to deduce the origins of the air mass arriving at SSI in
193 adjacent region. Generally, observed prevailing winds exhibited distinct seasonal
194 variabilities which were greatly affected by the East Asian monsoon. In warm seasons
195 (May-August), the site was predominately influenced by easterly and southeasterly winds,
196 accounting for 40–50% of the total winds. While in cold seasons (November-February),
197 the northwesterly and northerly winds became the predominant flows that affected SSI,
198 accounting for about 45% of total winds. During transitional months (e.g. March, April,
199 September and October), the dominant winds presented more diversities, with wind
200 directions dispersedly distributed in all the directions. The observed seasonal variations of
201 prevailing winds are typical at coastal cities at mid-latitude region (Shan et al., 2016; Xu et
202 al., 2019), suggesting that air masses arriving at SSI originated from various regions and
203 could result in different impacts on the offshore atmospheric composition in different
204 months.

205 Since CO has a relative long chemical lifetime of a few months, the observed CO
206 concentrations at DT could be regarded as a consequence of regional transport from
207 polluted regions (Tie et al., 2009). Figure 3 displays the observed monthly mean CO
208 mixing ratios under wind directions of north (N), northeast (NE), east (E), southeast (SE),
209 south (S), southwest (SW), west (W), and northwest (NW) at DT during the 2012–2017
210 period. Observed CO exhibited relative higher concentrations under SW and W winds in

211 all months, with mean mixing ratios of 0.44 and 0.56 ppmv, respectively during 2012–2017
212 (Table 1). The observed high CO mixing ratios suggested that the atmosphere
213 constituents at SSI could be more affected by regional transport of air pollutants under
214 SW and W wind conditions. As SSI is located to the northeast of the Shanghai city (Fig. 1),
215 air masses carried by the SW and W flows usually contain more urban pollutants from
216 upwind city areas, and those carried by E, SE, and NE flows mostly come from the ocean.
217 The oceanic air masses are less polluted compared to those from the cities, leading to
218 lower CO mixing ratio at SSI. For example, observed CO exhibited a mean concentration
219 of 0.23 ppmv under SE wind conditions, which was about 50% lower than that influenced
220 by W winds. To further examine the impacts of the SW and W winds on the atmosphere
221 constituents at SSI, Table 2 lists the calculated monthly mean occurrence frequency of the
222 SW and W winds in separate months during the studied period. The SW and S winds
223 were most infrequent in September (6.1 %) and October (5.2 %), suggesting that the
224 atmosphere at SSI during the two months could be less contaminated by pollutants
225 transported from the city and might be more close to the baseline oceanic air conditions.

226 3.2 The diurnal pattern of ozone at SSI

227 Figure 4 displays the monthly mean diurnal variations of O₃ at SSI and XJH in different
228 months during 2012–2017. The observed O₃ concentrations at the two sites exhibited
229 similar seasonal variations, with monthly mean values highest (61.4 ppbv for SSI and 35.9
230 ppbv for XJH) in May and lowest (33.4 ppbv for SSI and 12.5 ppbv for XJH) in December.
231 Since the O₃ formation in urban Shanghai is VOC-limited, observed O₃ could be
232 significantly depressed by large NO_x emissions at downtown site (XJH) (Gu et al., 2020).

233 In Fig. 4, observed O₃ levels at XJH were quite lower than those at SSI in all months, with
234 mean concentrations of 27.8 and 50.1 ppbv, respectively at XJH and SSI during the
235 observation period. The observed mean daily maximum 8-h average (MAD8) O₃
236 concentrations exhibited same differences between the two sites, which were 40.1 and
237 62.0 ppbv, respectively at XJH and SSI. The observed mean O₃ concentration at SSI was
238 also higher than that at DT (44.7 ppbv, Fig. S1) which is more close to the city, suggesting
239 that O₃ levels in marine air could be higher than those at continental urban and rural sites.
240 The observed diurnal patterns of O₃ at SSI and XJH in Fig. 4 were similar to those
241 reported for other sites in eastern China (Xu et al., 2008; Geng et al., 2015; Gao et al.,
242 2017), exhibiting minimums in early morning (06:00–08:00 LST) and maximums in the
243 afternoon (13:00–15:00 LST). However, compared to those at the urban site (XJH),
244 observed amplitudes of O₃ diurnal variations were much smaller at SSI. The diurnal
245 variations of surface O₃ can be mainly attributed to the O₃ production through
246 photochemical reactions in the daytime and O₃ depression via NO titration at nighttime
247 (Sillman, 2003). Due to few emissions of O₃ precursors (NO_x and VOCs), the O₃
248 production and depression could be weaker at remote site, resulting in flatter diurnal cycle
249 of O₃ compared to that at polluted urban site.

250 Since the amplitudes of O₃ diurnal variations usually exhibited much smaller values in
251 background areas compared to those in polluted urban regions, the ratio of daily
252 maximum O₃ concentration (O_{3-max}) to minimum O₃ concentration (O_{3-min}) was regarded as
253 an indicator to identify if the local O₃ pollution was significantly influenced by
254 anthropogenic emissions (Cvitac and Klasinc 1993; Vingarzan, 2004). The O_{3-max}/O_{3-min}

ratio displayed larger values in polluted regions (Cvitac et al., 1995) and lower values in less contaminated rural regions. A ratio of about 1.4 suggested that the site could be regarded as a typical background site (Scheel et al., 1997). For regional background sites in China, the typical values of $O_3\text{-max}/O_3\text{-min}$ were usually in the range of 2–3 (Xu et al., 2008; Meng et al., 2009; Gu et al., 2020). In Lin'an, a continental background site in YRD region, the ratio was reported to increase as a result of NO_x emission changes during past decades, which could reach above 6 during summertime (Xu et al., 2008). In Fig. 4, observed O_3 displayed different diurnal variabilities in various months at SSI. The variations of the $O_3\text{-max}/O_3\text{-min}$ ratio suggested different influence of regional transport on O_3 levels in the marine atmosphere.

Figure 5 displays the calculated monthly mean $O_3\text{-max}/O_3\text{-min}$ ratios at SSI and XJH, respectively during 2012–2017. Generally, the observed ratios of $O_3\text{-max}/O_3\text{-min}$ at SSI were much lower than those at XJH in all the months, suggesting less impact of anthropogenic emissions on O_3 levels. The calculated mean ratios were 3.03 and 5.20, respectively at SSI and XJH, and most of the calculated values were larger than 4.50 at the urban site. Besides, the ratios presented distinct seasonal differences at XJH and SSI sites. Higher values were observed in summer, indicating stronger photochemical production of daytime O_3 during June to August. At SSI, the $O_3\text{-max}/O_3\text{-min}$ ratio exhibited relatively low values in September and October, ranging from 1.61–2.35 during the studied period. The values were consistent with the typical values of $O_3\text{-max}/O_3\text{-min}$ observed at continental background sites in China (Xu et al., 2008; Meng et al., 2009; Gu et al., 2020). Since the observed temperature and solar radiation still exhibited higher values during the two

277 months in Shanghai (Gao et al., 2017), the observed low O₃ diurnal amplitudes should not
278 be attributed to the weakened photochemical formation of O₃ as those in winter. Due to
279 the persistent control of anticyclone, Shanghai and its neighboring areas are usually
280 dominated by stable weather conditions in September and October, resulting in more
281 gentle and diversified wind conditions. During the two months, the occurrences of more
282 polluted SW and W winds were lowest (6.1% and 5.2%) throughout the year. The
283 corresponding wind speed (2.49 and 2.50 m s⁻¹) also exhibited values 20% lower those in
284 other months (Table 2). The transport conditions led to fewer pollutants transported to the
285 SSI region, which could explain the observed weak diurnal variabilities of O₃ in September
286 and October. The transport conditions together with O₃ response further confirmed that
287 the transport of city pollutants had minimum impacts on the offshore O₃ levels in oceanic
288 air at SSI in September and October, providing a good proxy to study the baseline oceanic
289 O₃ and oxidation capacity of background atmosphere in eastern China.

290 3.3 Overall changes of ozone in oceanic air at SSI

291 Several studies have observed increasing trends of ground-level O₃ in metropolitan areas
292 over eastern China since 2013, suggesting that the O₃ increases were mostly attributed to
293 the NO_x emission reductions (Ma et al., 2016; Gao et al., 2017; Lu et al., 2018; Li et al.,
294 2019b). However, the O₃ changes at remote sites were relatively not well elucidated
295 during past years. Figure 6a presents the monthly variations of O₃ concentrations at SSI
296 and XJH during the 2012–2017 period. The statistical results of the MK test and Theil–
297 Sen trend estimate method indicated that observed monthly mean O₃ mixing ratios (O_{3-ave})
298 exhibited increasing changes at both urban (XJH) and remote sites (SSI) in Shanghai,

299 with calculated increasing rate of 1.97 and 1.12 ppbv yr^{-1} , respectively in XJH and SSI.
300 Though an overall upward trend of O_3 was detected at SSI, the changes were not as
301 remarkable as those observed at XJH, which could not even pass the MK trend test at the
302 90% confidence level. The monthly mean MDA8 and daily extreme values of O_3 exhibited
303 similar differences between the two sites. The calculated increasing rates of MDA8 O_3 ,
304 $\text{O}_{3\text{-max}}$ and $\text{O}_{3\text{-min}}$ were 2.73, 2.77, and 1.35 ppbv yr^{-1} ($\alpha < 0.05$), respectively at XJH, and
305 1.01, 1.35, and 1.27 ppbv yr^{-1} ($\alpha > 0.10$), respectively at SSI. Compared to the rapid O_3
306 increases in urban Shanghai which was suggested to mostly result from the significant
307 NO_x emission reductions in the past decade (Gao et al., 2017; Xu et al., 2019), the
308 statistically insignificant changes of O_3 detected at SSI indicated that O_3 in the oceanic air
309 remained a relative constant level during the study period and was less influenced by the
310 decreases of NO_x emissions.

311 As discussed in Sect. 3.1, the prevailing winds carried different levels of pollutants to
312 the SSI, resulting in different impacts on the O_3 levels in different months. In September
313 and October, the frequencies of SW and W winds that carried high levels of pollutants
314 were lowest (Table 1–2), exerting least influence on the atmospheric composition at SSI.
315 Therefore, the variations of surface O_3 concentrations in September and October at SSI
316 were examined to further assess the changes of least contaminated O_3 in the oceanic air.
317 Figure 6b presents the overall changes of daily mean surface O_3 concentrations in
318 September and October at SSI and XJH, respectively during the six-year period. The
319 corresponding mean O_3 mixing ratios during the two months were 60.9 and 31.3 ppbv,
320 respectively at SSI and XJH. Compared to the significant elevated O_3 concentrations at

321 XJH (0.59 ppbv yr⁻¹, $\alpha<0.10$) in September and October, observed O₃ at SSI during same
322 months exhibited insignificant decreasing changes from 2017–2017. The changes (-0.72
323 ppbv yr⁻¹, $\alpha>0.10$) were somewhat different from the overall O₃ changes (+1.12 ppbv yr⁻¹,
324 $\alpha>0.10$) at SSI, suggesting different causes of the observed O₃ changes in the oceanic air
325 during September and October.

326 To investigate possible drivers of the observed changes in the least contaminated O₃
327 in September and October at SSI, Table 3 displays the statistical results of the MK test
328 and Theil-Sen trend estimate for NO_x and CO mixing ratios, temperature, and wind speed
329 during the 2012–2017 period. Statistically significant upward trends were detected in wind
330 speed, with estimated increasing rates of 0.21 m s⁻¹ yr⁻¹ during the observation period
331 ($\alpha<0.05$). The significantly enhanced surface wind speeds were conducive to the diffusion
332 of O₃, which might be an important meteorological driver of the observed decreasing
333 changes in O₃ levels at SSI from 2012 to 2017. Observed NO_x and CO levels exhibited
334 increases of 0.48 ppbv yr⁻¹ ($\alpha<0.05$) and 2.67 ppbv yr⁻¹ ($\alpha>0.10$), respectively in
335 September and October during the six-year period, indicating enhanced transport of
336 pollutants to the oceanic area. Tie et al. (2013) suggested that the VOC-limited regime of
337 O₃ formation was not only confined in urban Shanghai, but also extended to a broader
338 regional area surrounding Shanghai. Thus, the elevated NO_x concentrations might not
339 only retard daytime O₃ production but also enhance nighttime O₃ depression at SSI.

340 Figure 6c further presents corresponding variations of daytime (10:00-16:00 LST) and
341 nighttime (23:00-04:00 LST) mean O₃ concentrations at SSI. Both daytime and nighttime
342 O₃ concentrations exhibited downward changes, reflecting the O₃ response to the

343 enhanced O_3 diffusion and depression in September and October. Therefore, the
344 enhanced diffusion and depression of O_3 induced by the elevated wind speed and NO_x
345 concentrations might be important causes of the observed O_3 changes in September and
346 October at SSI. It should be noted that the influence of radiation cannot be analyzed since
347 observations of solar radiation were not available during the study period. Therefore, more
348 measurements are still needed to further understand the O_3 changes and corresponding
349 drivers in the oceanic air.

350 3.4 Impacts of urban plumes on ozone in oceanic air at SSI

351 Due to the relatively long residence lifetime (about one month), O_3 produced at urban
352 regions could be transported several hundred kilometers away to downwind areas.
353 Meanwhile, the urban plumes become more aged with continuous production/depletion of
354 O_3 and its precursors, resulting in non-linear changes in O_3 in downwind areas (Geng et
355 al., 2011; Tie et al., 2009, 2013). Several studies suggested that there tended to be
356 considerable O_3 formations in aged urban plumes in the downwind region of Shanghai
357 (Geng et al., 2011; Tie et al., 2013). To investigate the impacts of urban plumes on the O_3
358 levels in oceanic air at SSI, the relationships between observed O_3 and NO_x under
359 different wind conditions at SSI and DT are investigated in this section.

360 Figure 7 presents the daytime and nighttime O_3/NO_x -wind relationships in MAM
361 (March–May), JJA (June–August), SON (September–November), and DJF (December–
362 February), respectively during 2012–2017. The SW and W winds were associated with
363 higher NO_x concentrations in both daytime and nighttime. The result was consistent with
364 the observed CO changes in Sect. 3.1. Since there is no local anthropogenic emission at

365 SSI, the higher levels of NO_x and CO were mainly resulted from the transport of more
366 polluted urban plumes by the SW and W winds. Generally, observed daytime O_3 and NO_x
367 concentrations presented opposite variations with the wind direction changes (Fig. 7a). In
368 SON and DJF, the correlation coefficients (R_s) between daytime O_3 and NO_x were -0.72
369 and -0.75, respectively, indicating that the O_3 formation was inhibited by increased NO_x
370 concentrations. The results are in accordance with Tie et al. (2013) and Xu et al. (2019),
371 who suggested that Shanghai and a broader regional area surrounding the city were all in
372 the VOC-limited O_3 formation regime during the study period. However, in MAM and JJA,
373 the daytime O_3 - NO_x variations presented totally different patterns under SW and W wind
374 conditions. As wind directions turned from E-SE to SW-W, observed mean NO_x
375 concentrations increased from about 10 ppbv to 20 ppbv, while observed mean O_3
376 concentrations increased from 50–60 ppbv to 70–80 ppbv. The enhancements in daytime
377 O_3 levels suggested that there should be persistent production of O_3 in the polluted air
378 masses carried by the SW and W winds in MAM and JJA.

379 Based on observations and WRF-Chem simulations, Tie et al. (2013) suggested
380 considerable O_3 production in aged city plumes in the downwind area of Shanghai. Since
381 air masses affecting SSI site were directly originated from Shanghai under the SW and W
382 wind conditions (Fig. 1), the observed O_3 enhancements should be mainly attributed to the
383 O_3 production in the city plumes carried by SW and W winds. Studies during the
384 MIRAGE-Shanghai campaign suggested several factors that contributed to the O_3
385 enhancements in aged city plumes downwind Shanghai. First, as there is a large area of
386 forest located in the south of Shanghai, Geng et al. (2011) suggested that continuous

387 oxidation of isoprene emitted by the biogenic sources could result in enhanced production
388 of hydrogen radicals (HO_2) especially in warm seasons. Once the air massed were
389 transported north and mixed with high NO_x emissions, O_3 would be quickly produced.
390 However, the impacts of biogenic emissions on O_3 production were mainly limited in the
391 south part of Shanghai, which can hardly influence the atmosphere in the SSI region.
392 Then, Tie et al. (2013) further illustrated that the OH reactivity of alkane, alkene, aromatics,
393 and oxygenated VOCs (OVOCs) contributed to the O_3 formation in city plumes. Among
394 them, the influence of alkane, alkene and aromatics mostly occurred within or near the city,
395 while the OVOCs could be produced or emitted during the transport of the city plumes,
396 resulting in substantial O_3 enhancements in aged city plumes at 100–200 km downwind
397 Shanghai.

398 The SSI is located approximately 100 km northeast from the downtown area of
399 Shanghai. In MAM and JJA, the SW and W winds carried air masses with enhanced
400 OVOCs oxidation and O_3 production, resulting in elevated daytime O_3 levels on the island.
401 While in SON and DJF, the observed O_3 decreases at SSI during SW and W winds
402 suggested lower efficiency of O_3 productivity in the city plumes. That might be because
403 that fewer OVOCs were released or produced downwind the city due to the lower
404 temperature and weaker solar radiation (Cai et al., 2009). In addition, in SON and DJF, the
405 SW and W winds were usually related to low pressure system with large cloud cover and
406 rich water vapor in Shanghai, which could also lead to depressed photochemical reactions
407 and decreased O_3 levels. At night, observed O_3 and NO_x displayed totally opposite
408 changes with wind directions (Fig. 7b), indicating O_3 depression by nighttime NO_x titration

409 in all the seasons. High O_3 levels were observed under northeasterly, easterly and
410 southeasterly oceanic wind conditions, ranging from 50–60, 30–55, 55–60, and 40–50
411 ppbv respectively at night in MAM, JJA, SON, and DJF.

412 3.5 Impacts of offshore ozone on urban ozone air quality in Shanghai
413 As is presented in Sect. 3.2 and 3.3, observed O_3 concentrations at SSI were much higher
414 than those at urban site (XJH), suggesting higher levels of O_3 in oceanic air than those on
415 the continent. Therefore, sea breezes tend to bring more O_3 to the continent, aggravating
416 O_3 pollution in coastal cities. Shanghai is one of the largest cities located on the east coast
417 of China, experiencing severe O_3 pollution in recent years (Xu et al., 2019; Gu et al.,
418 2020). According to the cluster analysis results (Fig. S2), easterly winds from the ocean
419 greatly affected the Shanghai region, accounting for 64–78% of the total flows in
420 non-winter months during the period 2012–2017. To understand the impacts of higher O_3
421 in oceanic air on the urban air quality, numerical experiments are conducted using the
422 WRF-Chem model to examine the response of O_3 levels in Shanghai to various oceanic
423 air inflow conditions in this section.

424 Simulations are performed during September 1–30 2014 when the prevailing winds
425 were mostly northeasterly and easterly in the Shanghai region. The occurrence
426 frequencies of the northeasterly and easterly winds were 23% and 27% respectively,
427 during the simulation period, suggesting dominant influence of the oceanic air inflows on
428 the city of Shanghai. Consistent with above analysis, observed air O_3 concentrations were
429 much higher in oceanic regions than those in city areas, with monthly mean values of 30.9
430 and 57.7 ppbv, respectively at XJH and SSI in September 2014. The chemical boundary

431 conditions (BCs) of the regional model can represent the inflows conditions to explore
432 their impacts on surface concentrations of air pollutants over a certain continent region.
433 Using this method, Pfiter et al. (2011) proposed that chemical inflows taken from different
434 observational and model datasets could result in differences of ± 15 ppbv in O_3 levels in
435 the US west coast region. Therefore, three sets of numerical experiments are conducted
436 as follows to access the impacts of oceanic O_3 air inflows on the urban O_3 air quality in
437 Shanghai. All the simulations are driven by the same emissions, initial conditions, physical
438 and chemical schemes.

439 (1) BC_40: O_3 concentrations at the eastern lateral boundary of the domain on the
440 ocean are assigned to 40 ppbv, which is provided by the MOZART-4 model, closed to the
441 observed urban O_3 levels (29.0–38.4 ppbv) in Shanghai in September. The chemical BCs
442 are updated every 6 hours.

443 (2) BC_50: Same as BC_40, but with O_3 concentrations setting to 50 ppbv at the
444 eastern lateral boundary of the domain.

445 (3) BC_60: Same as BC_40, but with O_3 concentrations at the eastern lateral
446 boundary of the domain setting to 60 ppbv according to the observed O_3 levels at SSI
447 (50.9–71.0 ppbv) in September.

448 Figure 8 displays the simulated and observed monthly mean distributions of surface
449 O_3 concentrations in BC_40, BC_50 and BC_60 scenarios, respectively. In addition to the
450 observations at XJH and SSI, O_3 measurements obtained from other three sites, Pudong
451 (PD, suburban), Sheshan (SS, rural), and Dongtan (DT, rural), during the same period
452 were introduced to evaluate the model's performance in simulating O_3 in Shanghai. The

453 O_3 concentrations at all the sites were measured using the same method as described in
454 Sect. 2.1. The calculated distributions of O_3 agree with observations, which exhibit lower
455 values in urban regions compared to those in rural and ocean areas, indicating strong O_3
456 depressions in the city of Shanghai due to the VOC-limited O_3 formation regime. The R
457 values between the simulated and observed O_3 concentrations are all larger than 0.50 at
458 continental sites (XJH, PD, SS, and DT), suggesting good prediction of O_3 variations by
459 the model.

460 Table 4 displays the statistical results of the comparisons between the simulated and
461 observed surface O_3 concentrations at different sites in Shanghai. Generally, the
462 WRF-Chem model underestimates O_3 concentrations at all the sites in most cases. Taken
463 the BC_40 scenario for example, the O_3 concentrations are underestimated by 9.4–27.6%
464 at continental sites and 36.1% at SSI, suggesting larger underestimation of O_3
465 concentrations in oceanic regions. Model results further suggest that elevated O_3 levels in
466 the eastern chemical BCs would lead to increases in O_3 concentrations at both urban and
467 remote sites when the prevailing winds are mostly easterly in Shanghai. With O_3
468 concentrations increasing from 40 to 60 ppbv in the easterly oceanic air inflows, the
469 simulated monthly mean O_3 concentrations increase by 7.0–9.7 ppbv at continental sites
470 and 10.4 ppbv at SSI. The underestimation of O_3 levels by the model is also greatly
471 improved in the BC_60 scenario, when the chemical BCs of O_3 are more close to the
472 observations. Compared to those in the BC_40 scenario, the normalized mean bias
473 (NMBs) of the predicted O_3 concentrations reduced at most sites in the BC_60 scenario,
474 for example from -36.1 % to -18.1 % at SSI and -27.6% to -4.6% at XJH, suggesting a

475 crucial role of the eastern oceanic air inflows in influencing O₃ air quality in Shanghai.

476 The calculated monthly mean differences in surface O₃ concentrations between

477 simulations in different scenarios are further presented in Fig. 9. Since the dominant winds

478 are easterly during the simulation period, distinct changes in surface O₃ concentrations

479 throughout Shanghai are generated, exhibiting generally gradient increases from the

480 ocean to the continent as O₃ increases in the oceanic air inflows. With every 10 ppbv

481 increases in O₃ levels in oceanic air, the simulated surface mean O₃ concentrations

482 increase by 3–6 ppbv in the land area and 4–7 ppbv in the offshore region. Due to the

483 strong O₃ depressions associated with high anthropogenic emissions, the simulated O₃

484 enhancements are relatively lower in the central urban region compared to those in

485 surrounding areas. Even so, simulated mean O₃ concentrations still exhibit 6–8 ppbv

486 increases in downtown Shanghai in the BC_60 scenario, accounting for approximately 30%

487 of the simulated O₃ concentrations in the BC_40 case. During the period 2012–2017,

488 most of the measured O₃ concentrations ranged between 50–60 ppbv at SSI in non-winter

489 seasons. Carried by the easterly inflows, these oceanic air masses with higher O₃ levels

490 (50–60 ppbv) could be transported to the coastal regions, resulting in approximately 20–

491 30% increases in urban O₃ concentrations in Shanghai according to the sensitivity results.

492 4 Conclusions

493 In this paper, we present the first relatively long and continuous measurements of oceanic

494 air O₃ conducted at an offshore monitoring station on the Sheshan Island during January 1

495 2012 to September 15 2017. The southwesterly and westerly winds are proved to carry

496 more pollutants to the SSI site, exerting greater influence of human activities on the

497 oceanic atmosphere over the offshore region of the East China Sea. Since the two kinds
498 of winds exhibited minimum occurrence frequencies and wind speeds in September and
499 October, atmosphere at SSI during the two months are considered to be less affected by
500 the transport of regional pollution.

501 Compared to those in urban (XJH) and rural (DT) sites, the observed O₃ levels were
502 higher at SSI, with a mean value of 50.1 ppbv during the observation period. Similar
503 seasonal and diurnal patterns of O₃ were observed at SSI and XJH; however, the
504 amplitudes of O₃ variations were much smaller at the offshore site (SSI). Since O₃
505 formation in Shanghai and its surrounding regions were VOC-limited, the observational
506 results suggested that the production and depression of O₃ could be weaker in the ocean
507 regions due to weak influence of the anthropogenic emissions. Observed mean
508 O₃-max/O₃-min ratios also exhibited lower values at SSI (3.03) than those at XJH (5.20), with
509 minimum values ranging from 1.61–2.35 in September and October. The result further
510 illustrated that SSI was seldom affected by the anthropogenic emissions, especially in
511 September and October.

512 The multi-year changes of the oceanic O₃ at SSI are investigated using the
513 Mann-Kendall trend test and the Theil-Sen trend estimate method during 2012–2017.
514 Different from the significant O₃ increases detected at XJH and other rural sites reported
515 in previous studies, the observed mean O₃ concentrations at SSI exhibited statistically
516 insignificant increasing changes (1.12 ppbv yr⁻¹, $\alpha>0.10$) during the observation period
517 and insignificant decreasing changes (-0.72 ppbv yr⁻¹, $\alpha>0.10$) in September and October
518 when the transport of city pollutants had minimum impacts on the island. Due to fewer

519 impacts of anthropogenic emissions, most of the observed changes in O_3 at SSI could be
520 attributed to the changes of meteorological conditions. Observed wind speed exhibited
521 significant increases ($0.21 \text{ m s}^{-1} \text{ yr}^{-1}$, $\alpha < 0.05$) in September and October during the
522 observation period, suggesting that enhanced diffusion conditions could be an important
523 meteorological factor in determining the decreases in O_3 concentrations during the
524 observation period.

525 The impacts of urban plumes on O_3 levels in oceanic air at SSI are evaluated by
526 studying the relationships between observed O_3 and NO_x under different wind conditions.
527 The SW and W winds usually carried air masses with higher NO_x concentrations in both
528 daytime and nighttime to the island. Generally, observed daytime and nighttime O_3
529 concentration decreased as NO_x concentration increases in SW and W winds, exhibiting
530 typical VOC-limited characteristics of O_3 formation. The pattern was more typical in SON
531 and DJF, with R values of -0.72 and -0.75, respectively between O_3 and NO_x
532 concentrations. In MAM and JJA, the daytime O_3 - NO_x variations presented kind of
533 positive relationships under SW and W wind conditions, suggesting continuous O_3
534 production in aged city plumes from Shanghai. As reported in previous studies during the
535 MIRAGE-Shanghai campaign, enhanced OVOCS oxidation should be the most important
536 driver of the observed O_3 enhancements in the city plumes transported by the SW and W
537 winds.

538 The influence of the oceanic O_3 air inflows on urban O_3 air quality in Shanghai are
539 quantified during an easterly wind dominant episode (September 1–30, 2014). Numerical
540 experiments are conducted with chemical BCs of O_3 assigned according to different inflow

541 conditions using the WRF-Chem model. Model results suggest that increases of O₃ in the
542 easterly oceanic air inflows will lead to gradient increases from the ocean to the continent.
543 With every 10 ppbv O₃ increases, the calculated surface mean O₃ concentrations can
544 increase by 3–6 ppbv in the land and 4–7 ppbv in the offshore region. Compared to those
545 in surrounding regions, O₃ in central city of Shanghai exhibited lower enhancements in
546 response to the O₃ increases in oceanic air inflows due to strong O₃ depression processes.
547 Even so, the impacts of the oceanic air inflows can still lead to 20–30% increases in urban
548 O₃ concentrations which should be crucially considered in dealing with O₃ pollution in
549 large coastal cities like Shanghai.

550

551 *Data availability.* The data used in this paper can be provided upon request from Dr.
552 Jianming Xu (metxujm@163.com).

553

554 *Author contribution.* YG and JX came up with the original idea, designed the analysis
555 methods, developed the model code, and performed the simulations. WG provided the
556 observational data. YG and YQ conducted the analysis of the observations and model
557 results. YG prepared the manuscript with contributions from all co-authors.

558

559 *Competing interest.* The authors declare that they have no conflict of interest.

560

561 *Acknowledgements.* This work was supported by Shanghai Sailing program
562 (18YF1421200) and Science and Technology Commission of Shanghai Municipality

563 (Grand No. 19DZ1205003).

564 Reference

565 Cai, C., Geng, F., Tie, X. X., Yu, Q., and An, J.: Characteristics and source apportionment
566 of VOCs measured in Shanghai, China, *Atmos. Environ.*, 44, 5005–5014, 2010.

567 Chen, F. and Dudhia, J.: Coupling an advanced land surface hydrology model with the
568 Penn State-NCAR MM5 modeling system, Part I: Model implementation and
569 sensitivity, *Mon. Weather Rev.*, 129, 569–585, 2001.

570 Cvitas, T., and Klasinc, L.: Measurement of tropospheric ozone in the Eastern
571 Mediterranean, *Boll. Geofisico*, 16, 521–527, 1993.

572 Cvitas, T., Kezele, N., Klasinc, L., and Lisac, J.: Tropospheric ozone measurements in
573 Croatia, *Pure Appl. Chem.*, 67, 1450–1453, 1995.

574 Draxler, R. R. and Hess, G. D.: An overview of the HYSPLIT 4 modelling system for
575 trajectories, dispersion, and deposition, *Austral. Meteorol. Mag.*, 47, 295–308,
576 1998.

577 Dudhia, J.: Numerical study of convection observed during the winter monsoon
578 experiment using a mesoscale two-dimensional model, *J. Atmos. Sci.*, 46, 3077–
579 3107, 1989.

580 Emmons, L. K., Walters, S., Hess, P. G., Lamarque, J.-F., Pfister, G. G., Fillmore, D.,
581 Granier, C., Guenther, A., Kinnison, D., Laepple, T., Orlando, J., Tie, X., Tyndall,
582 G., Wiedinmyer, C., Baugcum, S. L., and Kloster, S.: Description and evaluation
583 of the Model for Ozone and Related chemical Tracers, version 4 (MOZART-4),
584 *Geosci. Model Dev.*, 3, 43–67, <https://doi.org/10.5194/gmd-3-43-2010>, 2010.

585 Fountoukis, C., and Nenes, A.: ISORROPIA II: a computationally efficient aerosol
586 thermodynamic equilibrium model for K^+ , Ca^{2+} , Mg^{2+} , NH_4^+ , Na^+ , SO_4^{2-} , NO_3^- ,
587 Cl^- , H_2O aerosols. *Atmos. Chem. Phys.* 7, 4639–4659, 2007.

588 Fu, Y., Liao, H., and Yang, Y.: Interannual and Decadal Changes in Tropospheric Ozone in
589 China and the Associated Chemistry-Climate Interactions: A Review, *Adv. Atmos.*
590 *Sci.*, 46, 452–460, 2019.

591 Gao, W., Tie, X., Xu, J., Huang, R., Mao, X., Zhou, G., and Chang, L.: Long-term trend of
592 O_3 , in a mega city (Shanghai), China: characteristics, causes, and interactions
593 with precursors, *Sci. Total Environ.*, 603–604, 425–433, 2017.

594 Geng, F., Mao, X., Zhou, M., Zhong, S., and Lenschow, D.: Multi-year ozone concentration
595 and its spectra in Shanghai, China, *Sci. Total Environ.*, 521–522, 135–143, 2015.

596 Geng, F., Tie, X., Guenther, A., Li, G., Cao, J., and Harley, P.: Effect of isoprene emissions
597 from major forests on ozone formation in the city of Shanghai, China, *Atmos.*
598 *Chem. Phys.*, 11, 10449–10459, 2011.

599 Gilbert, R.O.: *Statistical Methods for Environmental Pollution Monitoring*. John Wiley &
600 Sons, New York, USA, 1987.

601 Goodman, J. E., Prueitt, R. L., Sax, S. N., Pizzurro, D. M., Lynch, H. N., Zu, K., and
602 Venditti, F. J.: Ozone exposure and systemic biomarkers: evaluation of evidence
603 for adverse cardiovascular health impacts, *Crit. Rev. Toxicol.*, 45, 412–452, 2015.

604 Grell, G. A., Peckham, S. E., Schmitz, R., McKeen, S. A., Frost, G., Skamarock, W. C.,
605 and Eder, B.: Fully coupled “online” chemistry within the WRF model, *Atmos.*
606 *Environ.*, 39, 6957–6975, 2005.

607 Gocic, M., Trajkovic, S.: Analysis of changes in meteorological variables using
608 Mann-Kendall and Sen's slope estimator statistical tests in Serbia, *Global Planet.*
609 *Change*, 100, 172–182, 2013.

610 Gu, Y., Li, K., Xu, J., Liao, H., Zhou, G.: Observed dependence of surface ozone on
611 increasing temperature in Shanghai, China. *Atmos. Environ.*, 221, 117108, 2020.

612 Guenther, A., Karl, T., Harley, P., Wiedinmyer, C., Palmer, P. I., and Geron, C.: Estimates
613 of global terrestrial isoprene emissions using MEGAN (model of emissions of
614 gases and aerosols from nature), *Atmos. Chem. Phys.*, 6, 3181–3210, 2006.

615 Hong, S. Y. and Lim, J. O. J.: The WRF Single-Moment 6-Class Microphysics Scheme
616 (WSM6), *J. Korean Meteor. Soc.*, 42, 129–151, 2006.

617 IPCC: Climate Change 2013: The Physical Science Basis. Contribution of Working Group
618 I to the Fifth Assessment Report of the Intergovernmental Panel on Climate
619 Change, edited by Stocker, T. F., Qin, D., Plattner, G. K., Tignor, M., Allen, S. K.,
620 Boschung, J., Nauels, A., Xia, Y., Bex, V. and Midgley, P. M., Cambridge
621 University Press, United Kingdom and New York, USA, 2013.

622 Kendall, M.G.: Rank Correlation Methods, fourth ed., Charles Griffin, London, 1975.

623 Li, K., Jacob, D.J., Liao, H., Zhu, J., Shah, V., Shen, L., Bates, K.H., Zhang, Q., and Zhai,
624 S.: A two-pollutant strategy for improving ozone and particulate air quality in China.
625 *Nat. Geosci.* <https://doi.org/10.1038/s41561-019-0464-x>, 2019a.

626 Li, K., Jacob, D. J., Liao, H., Shen, L., Zhang, Q., and Bates, K.H.: Anthropogenic drivers
627 of 2013–2017 trends in summer surface ozone in China, *P. Natl. A. Sci. USA* 116
628 (2), 422–427, 2019b.

629 Li, M., Zhang, Q., Streets, D., He, K. B., Cheng, Y. F., Emmons, L. K., Huo, H., Kang, S. C.,
630 Lu, Z., Shao, M., Su, H., Yu, X., and Zhang, Y.: Mapping Asian anthropogenic
631 emissions of non-methane volatile organic compounds to multiple chemical
632 mechanisms. *Atmos. Chem. Phys.* 14, 5617–5638, 2014.

633 Lin, M., Horowitz, L. W., Cooper, O. R., Tarasick, D., Conley, S., Iraci, L. T., Johnson, B.,
634 Leblanc, T., Petropavlovskikh, I., and Yates, E. L: Revisiting the evidence of
635 increasing springtime ozone mixing ratios in the free troposphere over western
636 North America, *Geophys. Res. Lett.*, 42, 8719–8728,
637 <https://doi.org/10.1002/2015GL065311>, 2015.

638 Lin, Y. L., Farley, R. D., and Orville, H. D.: Bulk parameterization of the snowfield in a
639 cloud model, *J. Clim. Appl. Meteorol.*, 22, 1065–1092, 1983.

640 Lin, W., Xu, X., Zhang, X., Tang, J.: Contributions of pollutants from North China Plain to
641 surface ozone at the Shangdianzi GAW Station, *Atmos. Chem. Phys.*, 8, 5889–
642 5898, 2008.

643 Lou, S., Liao, H., Yang, Y., and Mu, Q., Simulation of the interannual variations of
644 tropospheric ozone over China: Roles of variations in meteorological parameters
645 and anthropogenic emissions, *Atmos. Environ.*, 122, 839–851, 2015.

646 Lu, X., Hong, J., Zhang, L., Cooper, O.R., Schults, M. G., Xu, X., Wang, T., Gao, M., Zhao,
647 Y., and Zhang, Y.: Severe surface ozone pollution in China: a global perspective,
648 *Environ. Sci. Technol. Lett.*, 5(8), 487, 194, 2018.

649 Ma, Z., Xu, J., Quan, W., Zhang, Z., Lin, W., and Xu, X.: Significant increase of surface
650 ozone at a rural site, north of eastern China, *Atmos. Chem. Phys.*, 16, 3969–3977,

651 2016.

652 Madronich, S., and Flocke, S.: The role of solar radiation in atmospheric chemistry, in:

653 Handbook of Environmental Chemistry, edited by Boule, P.. Springer, Heidelberg,

654 1–26, https://doi.org/10.1007/978-3-540-69044-3_1, 1999.

655 Mann, H.B.: Non-parametric tests against trend, *Econometrica* 13, 163–171, 1945.

656 Meng, Z. Y., Xu, X. B., Yan, P., Ding, G. A., Tang, J., Lin, W. L., Xu, X. D., and Wang, S. F.:

657 Characteristics of trace gaseous pollutants at a regional background station in

658 Northern China, *Atmos. Chem. Phys.*, 9, 927–936,

659 <https://doi.org/10.5194/acp-9-927-2009>, 2009.

660 Monks, P. S., Archibald, A. T., Colette, A., Cooper, O., Coyle, M., Derwent, R., Fowler, D.,

661 Granier, C., Law, K.S., Mills, G.E., Stevenson, D.S., Tarasova, O., Thouret, V., von

662 Schneidemesser, E., Sommariva, R., Wild, O., and Williams, M.L.: Tropospheric

663 ozone and its precursors from the urban to the global scale from air quality to

664 short-lived climate forcer, *Atmos. Chem. Phys.*, 15, 8889–8973, 2015.

665 Pfister, G. G., Parrish, D. D., Worden, H., Emmons, L. K., Edwards, D. P., Wiedinmyer, C.,

666 Diskin, G. S., Huey, G., Oltmans, S. J., Thouret, V., Weinheimer, A., and Wisthaler,

667 A.: Characterizing summertime chemical boundary conditions for airmasses

668 entering the US West Coast, *Atmos. Chem. Phys.*, 11, 1769–1790, 2011.

669 Scheel, H. E., Aresbough, H., Geiss, H., Gormiscek, B., Granby, K., Haszpra, L., Klasinc,

670 L., Kley, D., Laurila, T., Lindskog, A., Roemer, M., Schmitt, R., Simmond, P.,

671 Solberg, S., and Toupande, G.: On the spatial distribution and seasonal variation

672 of lower tropospheric ozone over Europe, *J. Atmos. Chem.*, 28, 11–28, 1997.

673 Schell, B., Ackermann, I., Hass, H., Binkowski, F. S., and Ebel, A.: Modeling the formation

674 of secondary organic aerosol within a comprehensive air quality model system, *J.*

675 *Geophys. Res.*, 106, 28275–28293, <https://doi.org/10.1029/2001JD000384>, 2001.

676 Sen, P. K.: Estimates of the regression coefficient based on Kendall's tau, *J. Am. Stat.*

677 *Assoc.*, 63, 1379–1389, 1968.

678 Shan, W., Yang, P., Lu, H., Ma, K., and Huang, Z.: Influence of Coastal Wind on Surface

679 Ozone and Nitrogen Oxides in Suburban Shanghai, *Asia-Pac. J. Atmos. Sci.*,

680 52(5), 451–458, 2016.

681 Sillman, S.: Photochemical Smog: Ozone and its Precursors, in: *Handbook of Weather,*

682 *Climate, and Water*, edited by Potter, T. and Bradley, R. R., John Wiley & Sons,

683 New York, USA, 227–242, 2003.

684 Stockwell, W. R., Middleton, P., Chang, J. S., and Tang, X.: The second generation

685 regional acid deposition model chemical mechanism for regional air quality

686 modeling, *J. Geophys. Res.-Atmos.*, 95, 16343–16367, 1990.

687 Tie, X., Brasseur, G., Emmons, L., Horowitz, I., and Kinnison, D.: Effects of aerosols on

688 tropospheric oxidants: a global model study, *J. Geophys. Res.-Atmos.*, 106,

689 22931–22964, 2001.

690 Tie, X., Geng, F., Guenther, A., Cao, J., Greenberg, J., Zhang, R., Apel, E., Li, G.,

691 Weinheimer, A., Chen, J., and Cai, C.: Megacity impacts on regional ozone

692 formation: observations and WRF-Chem modeling for the MIRAGE-Shanghai field

693 campaign, *Atmos. Chem. Phys.*, 13, 5655–5669, 2013.

694 Tie, X., Geng, F., Peng, L., Gao, W., and Zhao, C.: Measurement and modeling of O₃

695 variability in Shanghai, China: Application of the WRF-Chem model, *Atmos.*
696 *Environ.*, 43, 4289–4302, 2009.

697 Tie, X., Madronich, S., Li, G. H., Ying, Z.M., Weinheimer, A., Apel, E., and Campos, T.:
698 Simulation of Mexico City plumes during the MIRAGE-Mex field campaign using
699 the WRF-Chem model, *Atmos. Chem. Phys.* 9, 4621–4638, 2009.

700 Tie, X., Madronich, S., Walters, S., Rasch, P., and Collins, W.: Effect of clouds on
701 photolysis and oxidants in the troposphere, *J. Geophys. Res.*, 108, 4642, 2003.

702 Vingarzan, R.: A review of surface ozone background levels and trends, *Atmos. Environ.*,
703 38, 3431–3442, 2004.

704 Wang, T., Wei, X. L., Ding, A. J., Poon, C. N., Lam, Y. S., Li, Y. S., Chan, L. Y., and Anson,
705 M.: Increasing surface ozone concentrations in the background atmosphere of
706 Southern China, 1994–2007, *Atmos. Chem. Phys.*, 9, 6217–6227, 2009.

707 Wang, T., Xue, L., Brimblecombe, P., Lam, Y.-F., Li, L., and Zhang, L.: Ozone pollution in
708 China: A review of concentrations, meteorological influences, chemical precursors,
709 and effects, *Sci. Total Environ.*, 575, 1582–1596, 2017.

710 Wesely, M. L.: Parameterization of surface resistances to gaseous dry deposition in
711 regional-scale numerical models, *Atmos. Environ.*, 23, 1293–1304, 1989.

712 Xu, J., Tie, X., Gao, W., Lin, Y., and Fu, Q.: Measurement and model analyses of the
713 ozone variation during 2006 to 2015 and its response to emission change in
714 megacity Shanghai, China, *Atmos. Chem. Phys.*, 19, 9017–9035, 2019.

715 Xu, X., Lin, W., Wang, T., Yan, P., Tang, J., Meng, Z., and Wang, Y.: Long-term trend of
716 surface ozone at a regional background station in eastern China 1991–2006:
717 enhanced variability, *Atmos. Chem. Phys.*, 8, 2595–2607, 2008.

718 Xu, W., Lin, W., Xu, X., Tang, J., Huang, J., Wu, H., and Zhang, X.: Long-term trends of
719 surface ozone and its influencing factors at the Mt Waliguan GAW station, China –
720 part 1: overall trends and characteristics, *Atmos. Chem. Phys.*, 16, 6191–6205,
721 <https://doi.org/10.5194/acp-16-6191-2016>, 2016.

722 Yang, Y., Liao, H., and Li, J., Impacts of the East Asian summer monsoon on interannual
723 variations of summertime surface-layer ozone concentrations over China, *Atmos.*
724 *Chem. Phys.*, 14, 6867–6880, 2014.

725 Yue, X. and Unger, N.: Ozone vegetation damage effects on gross primary productivity in
726 the United States, *Atmos. Chem. Phys.*, 14, 9137–9153, 2014.

727 Table 1 Mean CO mixing ratios (ppmv) under north (N), northeast (NE), east (E),
728 southeast (SE), south (S), southwest (SW), west (W), northwest (NW) and calm (C) wind
729 conditions at Dongtan (DT) site, a remote rural site near the Sheshan Island (SSI) during
730 2012 to 2017.

	N	NE	E	SE	S	SW	W	NW	C
CO	0.31	0.27	0.25	0.23	0.27	0.44	0.56	0.38	0.34

731 Table 2 Monthly mean wind speeds (m s^{-1}) and occurrence frequencies (%) of the
732 southwest (SW) and west (W) winds at Dongtan (DT) site, a remote rural site near the
733 Sheshan Island (SSI) during 2012 to 2017.

	Jan.	Feb.	Mar.	Apr.	May	Jun.	Jul.	Aug.	Sep.	Oct.	Nov.	Dec.
SW+W	11.5	9.2	11.9	13.2	12.7	9.8	17.7	10.8	6.1	5.2	11.9	15.1
Wind speed	2.70	2.93	2.98	3.04	2.86	2.51	2.65	2.77	2.49	2.50	2.55	2.54

734 Table 3 Statistical results of the Mann-Kendall test and Theil-Sen trend estimate for daily
735 mean values of NO_x, CO mixing ratios, temperature (T), and wind speed (WS) in
736 September and October at Dongtan (DT) site, a remote rural site near Sheshan Island
737 (SSI) site during the 2012–2017 period. The units of the calculated slopes are ppbv yr⁻¹ for
738 NO_x and CO, °C yr⁻¹ for T, and m s⁻¹ yr⁻¹ for WS.

	NO _x	CO	T	WS
Slope Estimate	0.48*	2.67 ^Δ	0.15 ^Δ	0.21*

739 *The result is significant at the 95% confidence level.

740 ^ΔThe result cannot pass the Mann-Kendall trend test at the 90% confidence level.

741 Table 4 Statistical results of the comparisons between the simulated and observed
 742 surface O₃ concentrations at Sheshan (SS), Xujiahua (XJH), Pudong (PD), DT (Dongtan)
 743 and Sheshan Island (SSI) sites during September 2014. The calculated O₃ levels are
 744 obtained from BC_40, BC_50 and BC_60 simulations, respectively. Values of the average
 745 surface O₃ concentrations (Mean) and normalized mean bias (NMB) are displayed. The
 746 NMB is defined as $NMB = \frac{\sum_{i=1}^n (P_i - O_i)}{\sum_{i=1}^n O_i}$, where P_i and O_i are predicted and observed ozone
 747 mixing ratios for sample i , n is the number of total samples (numbers in parentheses).

	Cases	SS (681)	XJH (641)	PD (690)	DT (690)	SSI (720)
	Observation	39.7	30.4	40.3	46.4	57.7
Mean	BC_40	36.0	22.0	29.5	35.3	36.9
(ppbv)	BC_50	39.1	25.1	33.3	39.6	41.8
	BC_60	43.1	29.0	37.9	45.0	47.3
	BC_40	-9.4	-27.6	-26.7	-23.9	-36.1
NMB(%)	BC_50	-1.5	-17.5	-17.2	-14.5	-27.5
	BC_60	8.6	-4.6	-5.9	-3.0	-18.1

748 **Figure Captions**

749 **Figure 1** Land cover of Shanghai and corresponding locations and landscapes of Xujiahui
750 (XJH, urban), Dongtan (DT, rural) and Sheshan Island (SSI, remote and oceanic) stations.

751 **Figure 2** Monthly wind rose diagrams averaged over the period of 2012 to 2017 at
752 Dongtan (DT) site, a remote rural site near the Sheshan Island (SSI).

753 **Figure 3** Monthly mean CO mixing ratios under north (N), northeast (NE), east (E),
754 southeast (SE), south (S), southwest (SW), west (W), northwest (NW) and calm (C) wind
755 conditions at Dongtan (DT) site, a remote rural site near the Sheshan Island (SSI) during
756 2012 to 2017.

757 **Figure 4** Monthly and year-round mean diurnal variations of O_3 (ppbv) at Sheshan Island
758 (SSI, remote and oceanic) and Xujiahui (XJH, urban) sites during 2012 to 2017.

759 **Figure 5** Calculated monthly mean ratios of daily maximum O_3 concentrations ($O_{3\text{-max}}$) to
760 minimum O_3 concentrations ($O_{3\text{-min}}$) at Sheshan Island (SSI, remote and oceanic) and
761 Xujiahui (XJH, urban) sites, respectively during 2012 to 2017.

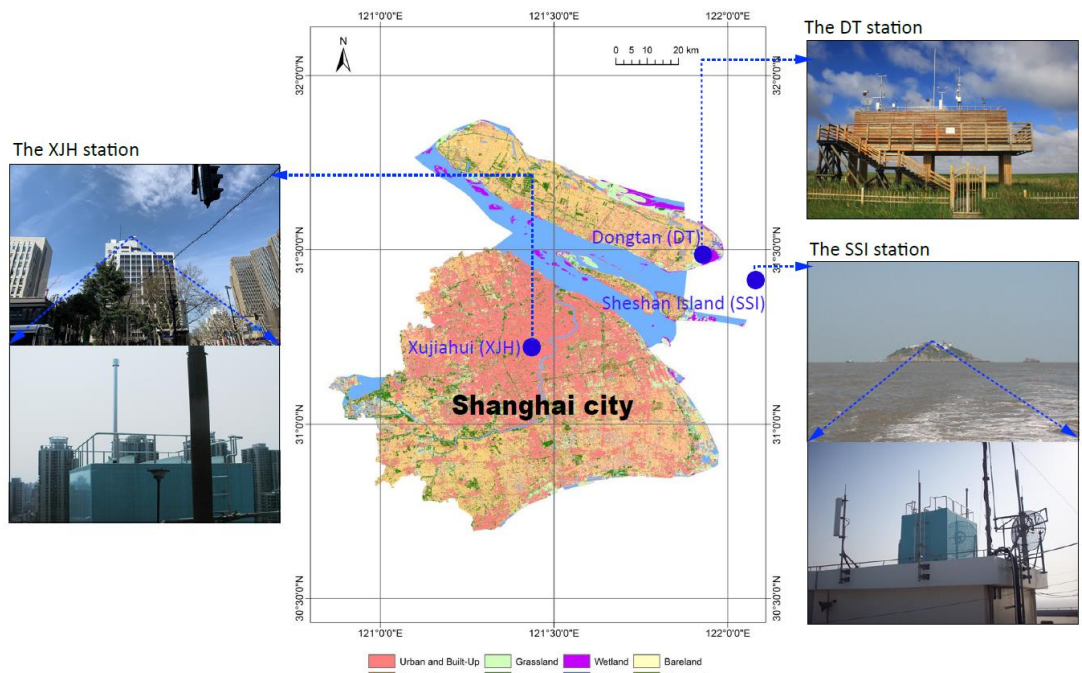
762 **Figure 6** Variations of (a) monthly mean O_3 concentrations at Sheshan Island (SSI,
763 remote and oceanic) and Xujiahui (XJH, urban) sites during the period 2012–2017, (c)
764 corresponding variations of daily mean O_3 concentrations at SSI and XJH in September
765 and October, and (c) variations of mean O_3 concentrations during daytime (10:00-16:00
766 LST) and nighttime (23:00-04:00 LST) at SSI.

767 **Figure 7** Daytime and nighttime mean O_3 mixing ratios (ppbv) at Sheshan Island (SSI)
768 and NO_x mixing ratios (ppbv) at Dongtan (DT) site, a remote rural site near SSI under
769 north (N), northeast (NE), east (E), southeast (SE), south (S), southwest (SW), west (W),

770 and northwest (NW) wind conditions in MAM (March–May), JJA (June–August), SON
771 (September–November), and DJF (December–February), respectively during 2012 to
772 2017.

773 **Figure 8** Calculated distributions of monthly mean O_3 concentrations (shades, ppbv) from
774 BC_40, BC_50 and BC_60 simulations, respectively in September 2014. Model results
775 are compared with observed mean O_3 concentrations (circles, ppbv) obtained from
776 Sheshan (SS), Xujiahua (XJH), Pudong (PD), DT (Dongtan) and Sheshan Island (SSI)
777 sites. Also shown is the calculated wind field ($m s^{-1}$) averaged over the same period.

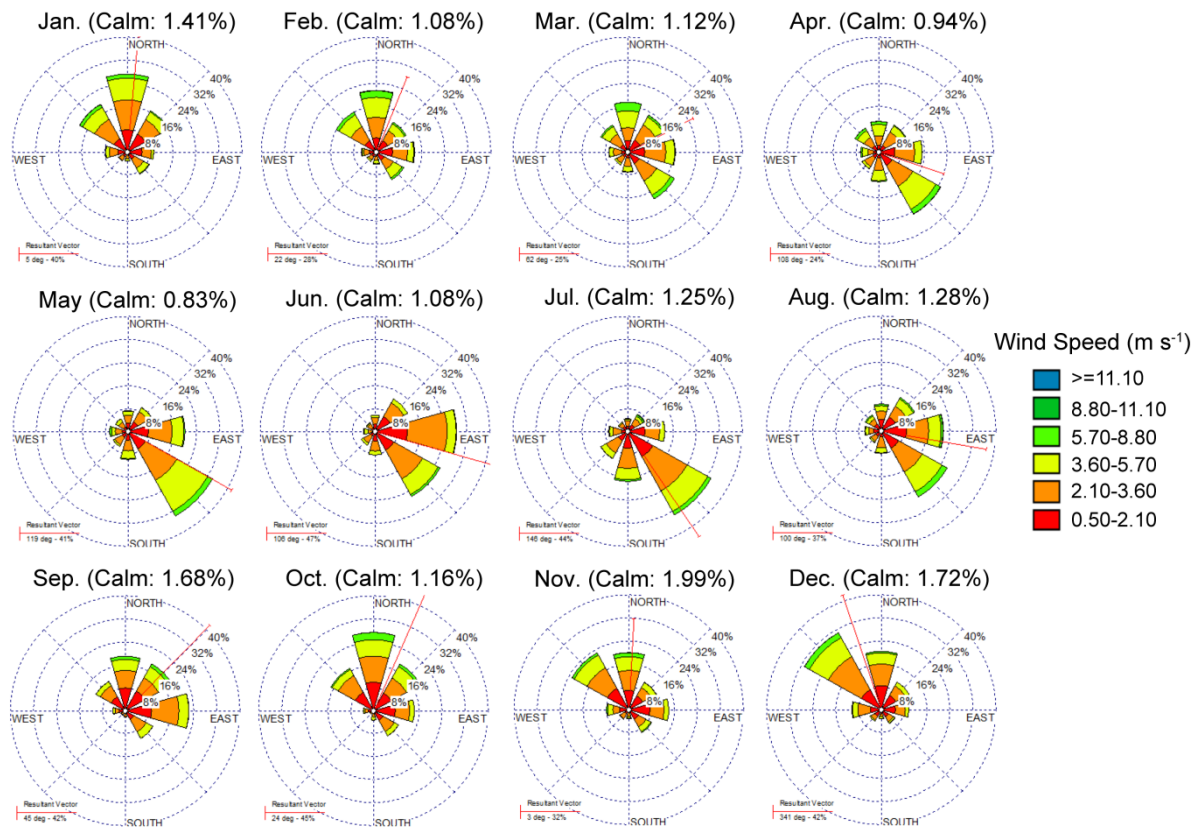
778 **Figure 9** Mean differences in surface O_3 concentrations (ppbv) simulated with different
779 chemical boundaries: (a) BC_50 minus BC_40, (b) BC_60 minus BC_40, and (c) BC_60
780 minus BC_50 in September 2014. Also shown is the calculated wind field ($m s^{-1}$) averaged
781 over the simulation period.



782

783 Figure 1 Land cover of Shanghai and corresponding locations and landscapes of Xujiahui

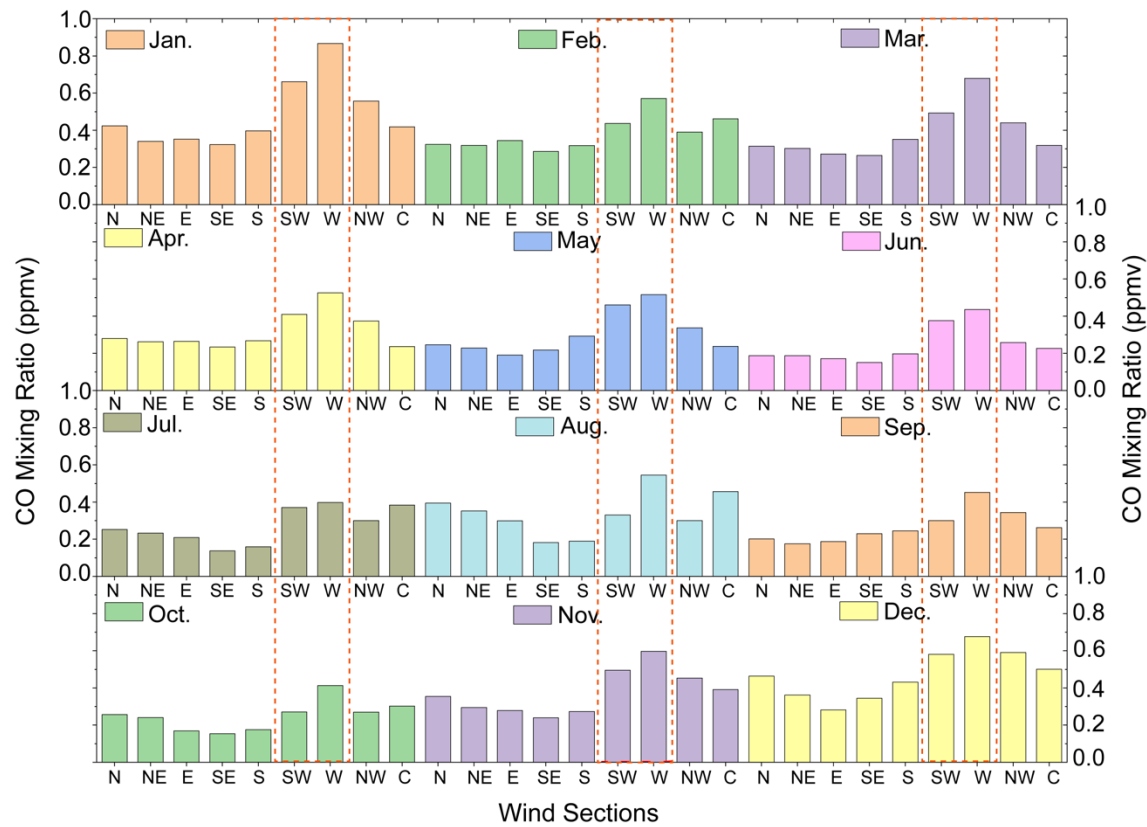
784 (XJH, urban), Dongtan (DT, rural) and Sheshan Island (SSI, remote and oceanic) stations.



785

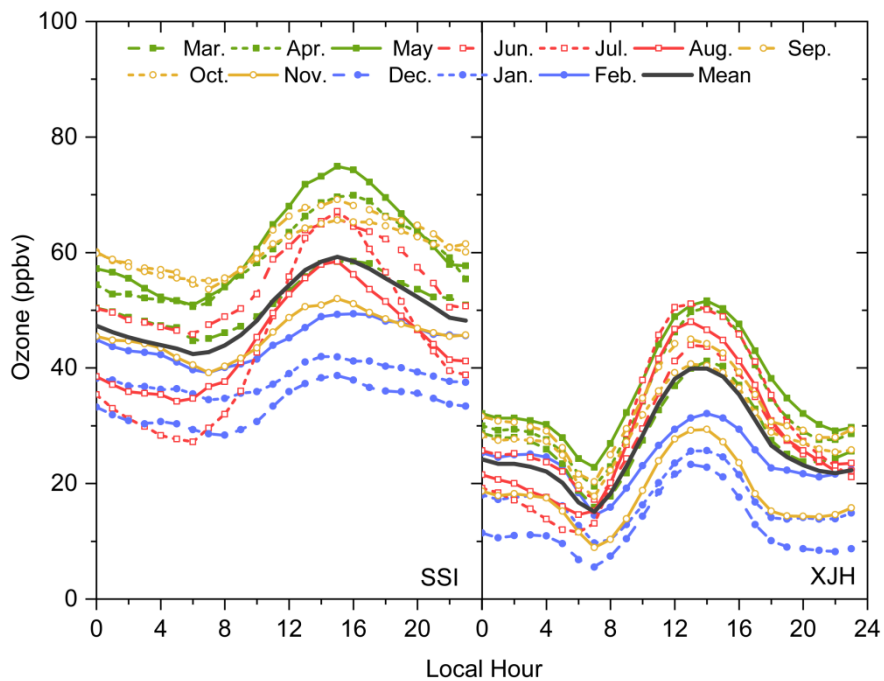
786 Figure 2 Monthly wind rose diagrams averaged over the period of 2012 to 2017 at

787 Dongtan (DT) site, a remote rural site near the Sheshan Island (SSI).



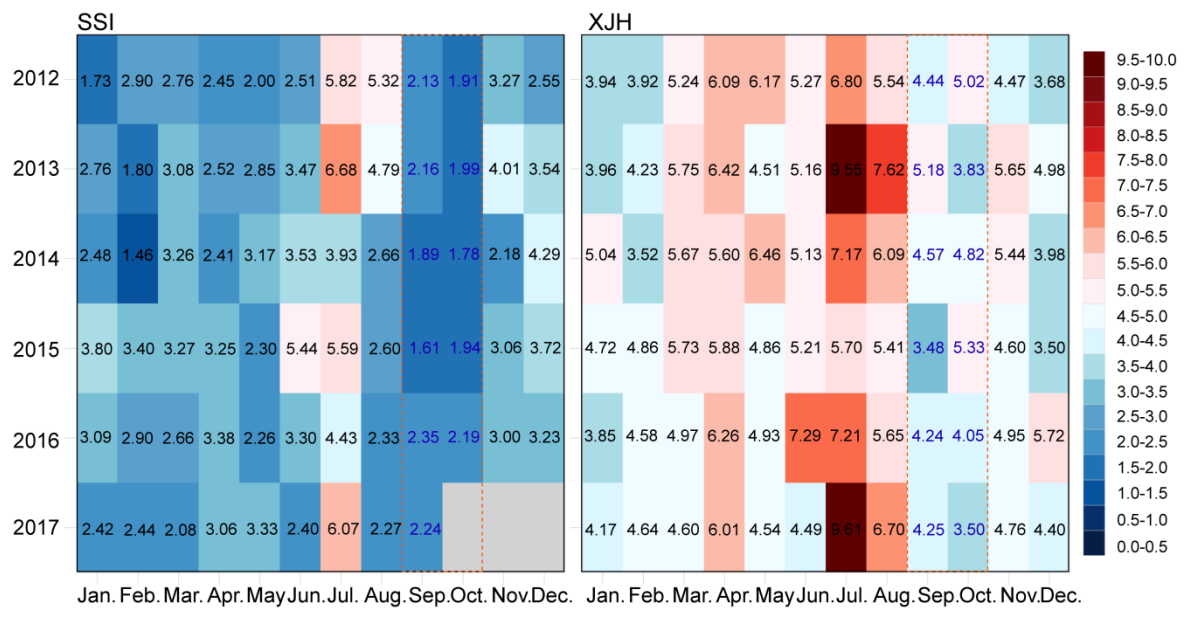
788

789 Figure 3 Monthly mean CO mixing ratios under north (N), northeast (NE), east (E),
 790 southeast (SE), south (S), southwest (SW), west (W), northwest (NW) and calm (C) wind
 791 conditions at Dongtan (DT) site, a remote rural site near the Sheshan Island (SSI) during
 792 2012 to 2017.



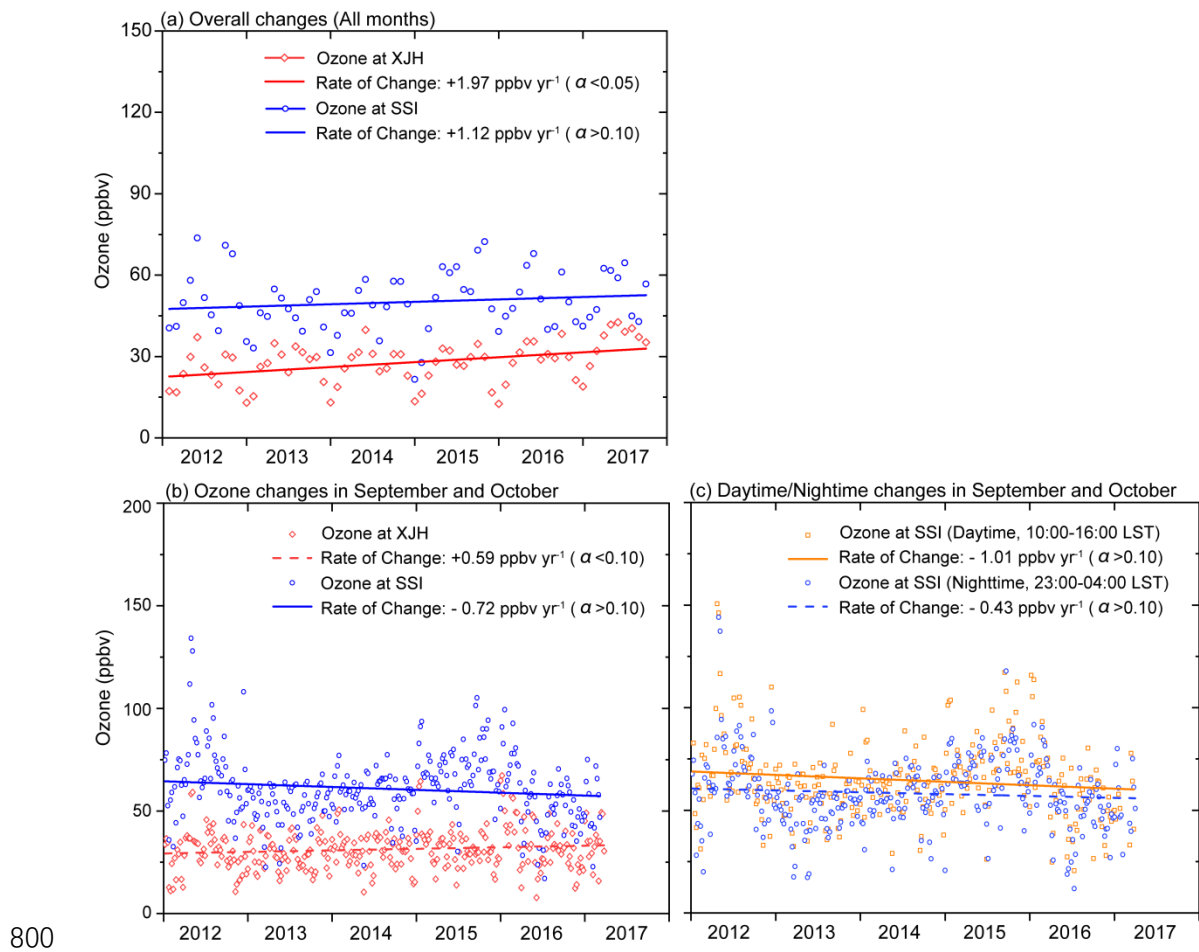
793

794 Figure 4 Monthly and year-round mean diurnal variations of O_3 (ppbv) at Sheshan Island
 795 (SSI, remote and oceanic) and Xujiahui (XJH, urban) sites during 2012 to 2017.

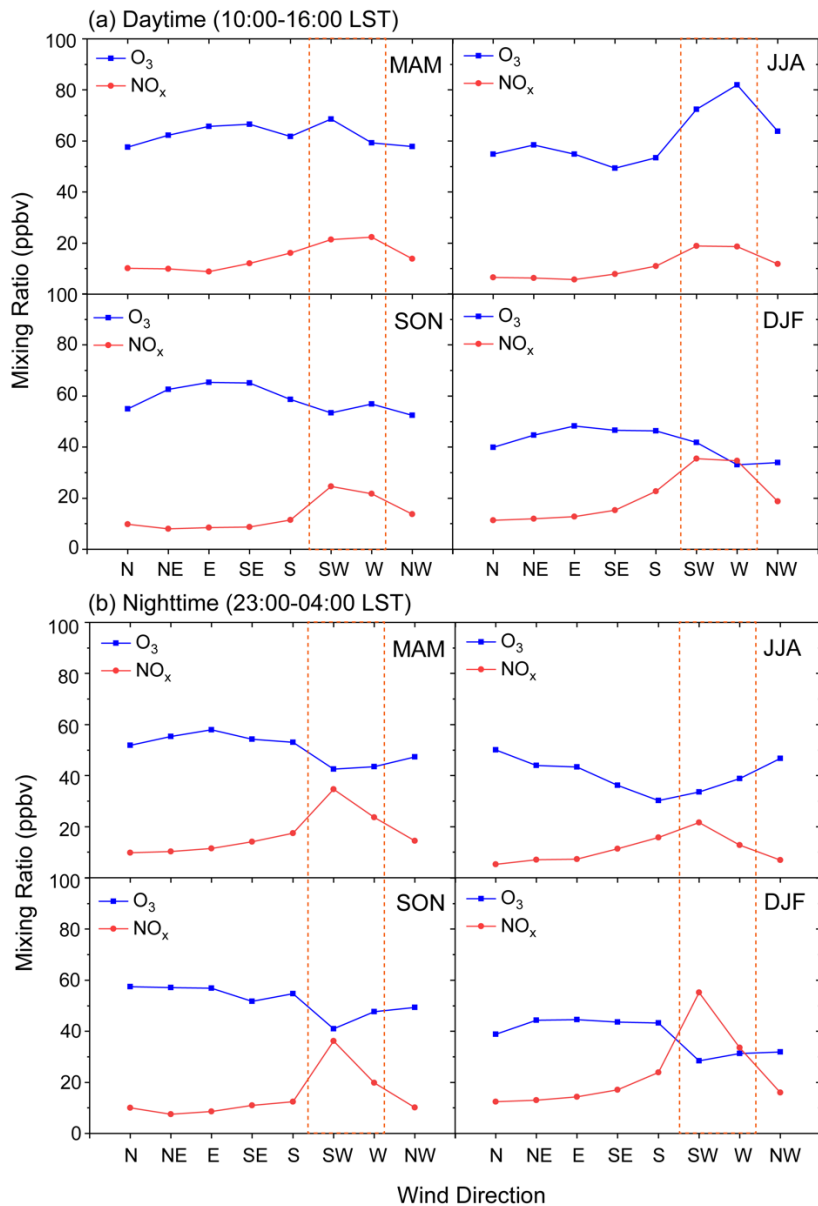


796

797 Figure 5 Calculated monthly mean ratios of daily maximum O₃ concentrations (O₃-max) to
 798 minimum O₃ concentrations (O₃-min) at Sheshan Island (SSI, remote and oceanic) and
 799 Xujiahui (XJH, urban) sites, respectively during 2012 to 2017.

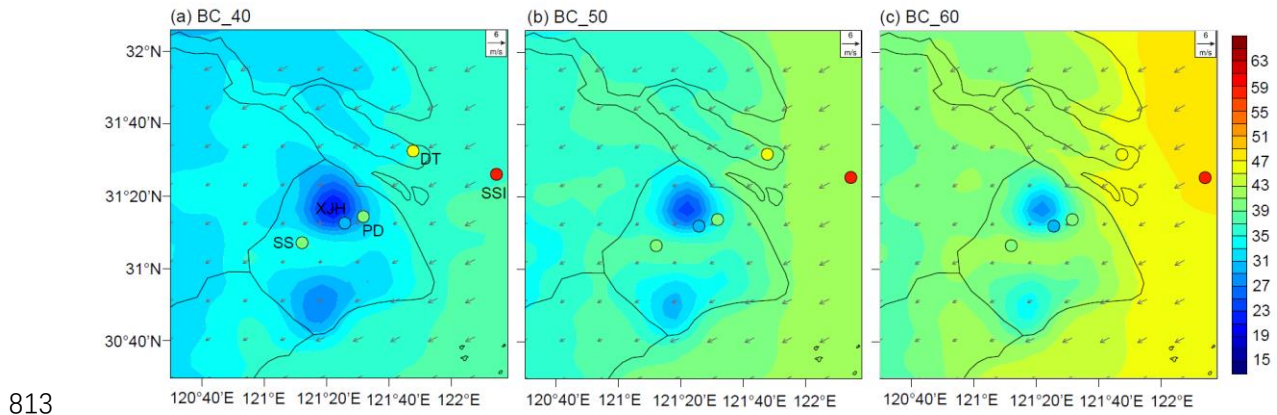


801 Figure 6 Variations of (a) monthly mean O₃ concentrations at Sheshan Island (SSI, remote
 802 and oceanic) and Xujiahui (XJH, urban) sites during the period 2012–2017, (b)
 803 corresponding variations of daily mean O₃ concentrations at SSI and XJH in September
 804 and October, and (c) variations of mean O₃ concentrations during daytime (10:00–16:00
 805 LST) and nighttime (23:00–04:00 LST) at SSI.



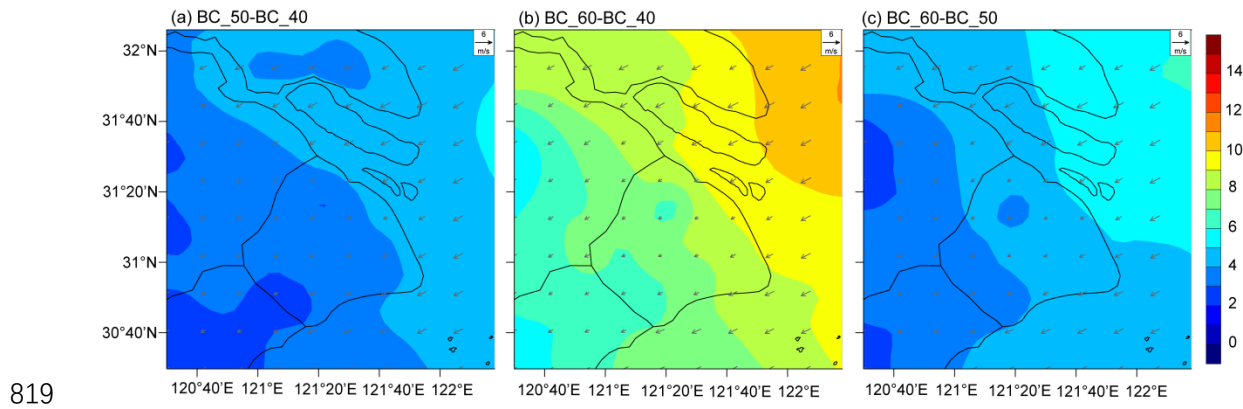
806

807 Figure 7 Daytime and nighttime mean O_3 mixing ratios (ppbv) at Sheshan Island (SSI) and
 808 NO_x mixing ratios (ppbv) at Dongtan (DT) site, a remote rural site near SSI under north (N),
 809 northeast (NE), east (E), southeast (SE), south (S), southwest (SW), west (W), and
 810 northwest (NW) wind conditions in MAM (March–May), JJA (June–August), SON
 811 (September–November), and DJF (December–February), respectively during 2012 to
 812 2017.



813

814 Figure 8 Calculated distributions of monthly mean O_3 concentrations (shades, ppbv) from
 815 BC_40, BC_50 and BC_60 simulations, respectively in September 2014. Model results
 816 are compared with observed mean O_3 concentrations (circles, ppbv) obtained from
 817 Sheshan (SS), Xujiahua (XJH), Pudong (PD), DT (Dongtan) and Sheshan Island (SSI)
 818 sites. Also shown is the calculated wind field ($m s^{-1}$) averaged over the same period.



819

820 Figure 9 Mean differences in surface O₃ concentrations (ppbv) simulated with different
 821 chemical boundaries: (a) BC_50 minus BC_40, (b) BC_60 minus BC_40, and (c) BC_60
 822 minus BC_50 in September 2014. Also shown is the calculated wind field (m s⁻¹) averaged
 823 over the simulation period.